communications physics

A Nature Portfolio journal

Article

https://doi.org/10.1038/s42005-025-02270-3

Bias-field digitized counterdiabatic quantum algorithm for higher-order binary optimization

Sebastián V. Romero [1,2], Anne-Maria Visuri [1], Alejandro Gomez Cadavid [1,2], Anton Simen [1,2], Enrique Solano [1] & Narendra N. Hegade [1]

Combinatorial optimization plays a crucial role in many industrial applications. While classical computing often struggles with complex instances, quantum optimization emerges as a promising alternative. Here, we present an enhanced bias-field digitized counterdiabatic quantum optimization (BF-DCQO) algorithm to address higher-order unconstrained binary optimization (HUBO). We apply BF-DCQO to a HUBO problem featuring three-local terms in the Ising spin-glass model, validated experimentally using 156 qubits on an IBM quantum processor. In the studied instances, our results outperform standard methods such as the quantum approximate optimization algorithm, quantum annealing, simulated annealing, and Tabu search. Furthermore, we provide numerical evidence of the feasibility of a similar HUBO problem on a 433-qubit Osprey-like quantum processor. Finally, we solve denser instances of the MAX 3-SAT problem in an IonQ emulator. Our results show that BF-DCQO offers an effective path for solving large-scale HUBO problems on current and near-term quantum processors.

Combinatorial optimization problems arise in a multitude of situations in science and industry, from logistics and scheduling to computational chemistry and biology. In combinatorial optimization, the best or near-optimal solution is searched within a finite but large discrete configuration space. Theoretical tools from statistical physics have given insights into these problems, as their connection to disordered systems was identified early on[1]. These problems generally belong to the NP-hard complexity class, requiring a computation time that grows exponentially with the problem size on classical computers. While complex problem instances test the limits of classical computing, quantum computing has emerged as a suitable counterpart to drive the state of the art in this field. This is possible due to the rapid development of quantum technologies combined with the natural mapping of combinatorial optimization problems to the widely studied Ising spin glass model, whose ground state encodes the optimal solution[2]. Several methods have been proposed so far, including adiabatic quantum optimization[3] and the quantum approximate optimization algorithm (QAOA)[4], which can be thought as a digitized version of adiabatic quantum computing[5].

In addition to the capacity of quantum hardware to embed large-scale systems, the potential of quantum computing to surpass classical optimization methods has been demostrated through dedicated quantum algorithms[6–13]. Among these, QAOA has emerged as one of the front-runner candidates for showing quantum speedup in optimization. Recent studies on 8-SAT problems with up to 20 variables[14] show that the time to solution for QAOA outperforms best-known classical methods. Similar evidence of quantum speedup for solving the low autocorrelation binary sequence (LABS) problem has also been found[15–17].

In parallel with quantum algorithms, quantum-inspired algorithms run on classical hardware, especially those based on tensor networks (TNs)[18–22], have evolved rapidly in the recent years. They were developed over the past three decades mostly for the study of condensed-matter physics[21,23] and have been adopted as efficient simulators of quantum hardware, as classical benchmarks for quantum algorithms, and in hybrid approaches combining TNs and quantum algorithms[24–27]. The recent kicked-Ising-model experiment of IBM on a 127-qubit device[28–32] and D-Wave's simulation of quantum quench dynamics across a spin-glass phase transition[33,34] highlighted the interplay of quantum simulations and TNs. For combinatorial optimization, new approaches have combined generative machine learning models with TNs[35–37], and ground-state search methods have been applied to problems with up to quadratic terms on higher-dimensional graphs[38–40].

Compared to quadratic problems, higher-order ones are significantly more difficult to solve. While a number of experiments have recently demonstrated higher-order unconstrained binary optimization (HUBO)

[1]Kipu Quantum GmbH, Berlin, Germany. [2]Department of Physical Chemistry, University of the Basque Country UPV/EHU, Bilbao, Spain.
e-mail: narendrahegade5@gmail.com

implementations on quantum hardware[41–44], there are hardware limitations that complicate the effective implementation of these protocols on large- and even intermediate-scale problems. These include short decoherence times, qubit connectivities, and the presence of noise. Several alternative methods, such as counterdiabatic driving (CD) protocols, have been proposed to overcome these issues[45–50]. By suppressing diabatic transitions, CD protocols can find better solutions in different scenarios.

In this work, we develop and exploit an improved version of the recently introduced bias-field digitized counterdiabatic quantum optimization (BF-DCQO) formulation[51] to address HUBO problems on both ideal simulators and hardware. We make use of the entire new 156-qubit IBM quantum computer IBM_FEZ and a matrix product state (MPS) simulation of the upcoming IBM Osprey processor with 433 qubits. To test BF-DCQO on denser instances, we consider a MAX 3-SAT problem at the critical density and employ the 25-qubit IONQ ARIA 1 emulator with a noise model. All results are compared with those obtained through well-established classical optimization methods as well as the D-Wave quantum annealing platform. Unlike these methods, BF-DCQO does not require additional qubits for mapping the initial HUBO problem into a quadratic one. Even though our work addresses problems with up to three-body terms, our method is equally applicable to higher-order optimization problems, including the LABS problem[17], MAX k-SAT[52], factorization[53] and protein folding[54,55], among others.

Methods

Digitized counterdiabatic quantum optimization (DCQO)

Adiabatic quantum optimization aims to prepare the ground state of a given problem Hamiltonian. An initial state is evolved within the time window $t \in [0, T]$ under the adiabatic protocol $H_{\rm ad}(\lambda) = (1-\lambda)H_i + \lambda H_f$. Here, $\lambda(t)$ is a time-dependent scheduling function that describes the adiabatic evolution of the system, starting from an initial Hamiltonian H_i, whose corresponding ground state is easy to prepare, towards the problem Hamiltonian H_f. Relying on the adiabatic theorem, this protocol reaches the desired ground state of H_f in the adiabatic limit $\dot{\lambda}(t) \to 0$. We consider the disordered Ising Hamiltonian with up to three-body terms:

$$H_f = \sum_i h_i^z \sigma_i^z + \sum_{i<j} J_{ij} \sigma_i^z \sigma_j^z + \sum_{i<j<k} K_{ijk} \sigma_i^z \sigma_j^z \sigma_k^z, \tag{1}$$

in contrast to Ref. 51, which only considers up to quadratic terms. We use here natural units with $\hbar = 1$. The ground state of this Hamiltonian is called a p-spin glass with $p = 3$[56], and the model is commonly known in quantum optimization as the higher-order Ising chain[41,42]. In the following, we use $\lambda(t) = \sin^2(\pi \sin^2(\pi t/2T)/2)$ as the scheduling function. The initial Hamiltonian is

$$H_i = \sum_j h_j^x \sigma_j^x + \sum_j h_j^b \sigma_j^z \tag{2}$$

with h_j^x (h_j^b) the transverse- (longitudinal bias-) field contributions acting on the jth spin. We set $h_j^x = -1$ and $h_j^b = 0$, thus $H_i = -\sum_{j=0}^{N-1} \sigma_j^x$, so that the N-qubit ground state of H_i is

$$|+\rangle^{\otimes N} = \left(\frac{|0\rangle + |1\rangle}{\sqrt{2}} \right)^{\otimes N}. \tag{3}$$

In order to overcome the intrinsic slow adiabatic evolution, it is possible to introduce an auxiliary counterdiabatic driving contribution which accelerates the original protocol and suppresses diabatic transitions[45,46]. The transitionless protocol takes the form

$$H_{\rm cd}(\lambda) = H_{\rm ad}(\lambda) + \dot{\lambda} A_\lambda, \tag{4}$$

where A_λ is the adiabatic gauge potential[57]. Nevertheless, its exact implementation is severely impractical due to its many-body structure and the necessity for the knowledge of the full energy spectrum. To overcome these issues, several approximate implementations have been proposed[57–61]. One such proposal is the approximation of the adiabatic gauge potential by a nested-commutator series expansion

$$A_\lambda^{(l)} = i \sum_{k=1}^{l} \alpha_k(t) \mathcal{O}_{2k-1}(t), \tag{5}$$

where $\mathcal{O}_0(t) = \partial_\lambda H_{\rm ad}$ and $\mathcal{O}_k(t) = [H_{\rm ad}, \mathcal{O}_{k-1}(t)]$. In the limit $l \to \infty$, this expansion converges to the exact gauge potential. The coefficients α_k are obtained by minimizing the action $S_l = {\rm tr}[G_l^2]$ with $G_l = \partial_\lambda H_{\rm ad} - i\left[H_{\rm ad}, A_\lambda^{(l)}\right]$. For simplicity, we consider the first-order ($l = 1$) nested-commutator term (see Supplementary Note 1 for a step-by-step derivation), which takes the form

$$\mathcal{O}_1 = -2i \Bigg[\sum_i h_i^z \sigma_i^y + \sum_{i<j} J_{ij} (\sigma_i^y \sigma_j^z + \sigma_i^z \sigma_j^y) + \sum_{i<j<k} K_{ijk} (\sigma_i^y \sigma_j^z \sigma_k^z + \sigma_i^z \sigma_j^y \sigma_k^z + \sigma_i^z \sigma_j^z \sigma_k^y) \Bigg]. \tag{6}$$

Higher-order terms demand significantly more computational resources, and their complexity increases with the system size.

In the fast evolution regime, the adiabatic term $H_{\rm ad}(\lambda)$ in Eq. (4) can be omitted, reducing the number of required quantum gates and thereby decreasing hardware noise, while still maintaining the quality of the solution[51,55,62,63]. This approach is adopted in the present study, where only the CD contribution is considered without compromising performance. The time evolution of such Hamiltonians remains a challenge on current analog quantum platforms, and may even be highly difficult due to the nonstoquasticity[64]. To address this issue, digitized counterdiabatic quantum protocols have been proposed for implementation on digital quantum computers[65]. The resulting time-evolution operator can be decomposed using a first-order Trotter-Suzuki decomposition[66] and digitized with a gate-based approach,

$$U(T,0) = \prod_{k=1}^{n_{\rm trot}} \prod_{j=1}^{n_{\rm terms}} \exp\left[-i \gamma_j(k\Delta t) \Delta t H_j \right], \tag{7}$$

where $H_{\rm cd}(t) = \sum_{j=1}^{n_{\rm terms}} \gamma_j(t) H_j$ is encoded in $n_{\rm terms}$ different Pauli operators H_j and $n_{\rm trot}$ are the Trotter steps considered with $\Delta t = T/n_{\rm trot}$. We use $T = 1$ in units of the inverse energy scale relevant for each problem as defined below, and $n_{\rm trot} = 3$, thus one effective Trotter step is implemented. The number of gates required for implementation is reduced by optimally decomposing the desired circuit following Refs. 67,68. Furthermore, we set a gate-cutoff threshold $\theta_{\rm cutoff}$ in our experiments, such that any term of Eq. (7) with an angle with absolute value below this threshold is discarded, thus if $|\gamma_j(k\Delta t)\Delta t | {\rm mod} 2\pi < \theta_{\rm cutoff}$ is met. The larger the $\theta_{\rm cutoff}$, the lower is the amount of resources that are required, but the obtained circuit expressivity is also lower. Therefore, it is crucial to select an appropriate value of this parameter to significantly reduce the amount of gates to implement without compromising the quality of the outcomes.

Bias-field updating protocol

State initialization is crucial for the performance of quantum optimization routines, where an initial state with a nonzero overlap with the desired final state is advantageous[69,70]. Several warm-starting techniques have been proposed, where a relaxed version of the problem is solved classically and its

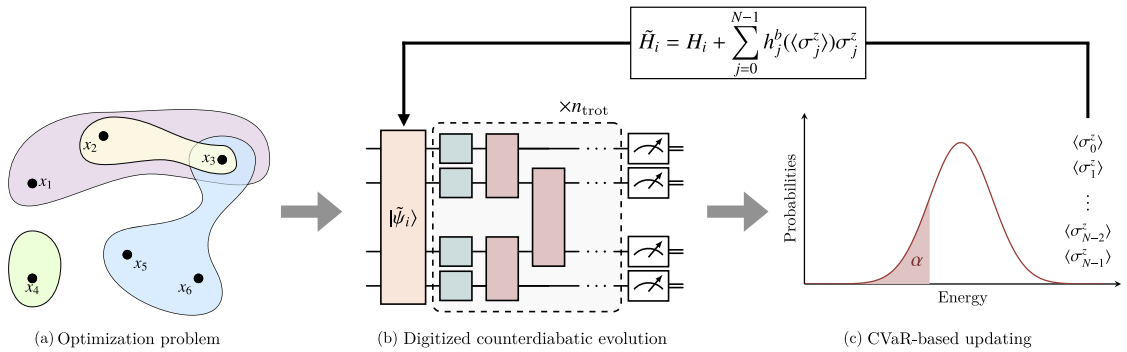

(a) Optimization problem (b) Digitized counterdiabatic evolution (c) CVaR-based updating

Fig. 1 | Schematic of the BF-DCQO protocol. Given a binary optimization problem of arbitrary order (depicted in (**a**)) encoded as a *p*-spin glass [Eq. (1)], the BF-DCQO algorithm performs DCQO iteratively, updating the input bias h_j^b from the solutions obtained from the previous step. Each iteration consists of running the corresponding DCQO circuit (depicted in (**b**)), sampling the final state, and updating the bias fields. It amounts to the use of (i) the CVaR-based approach, which considers only a subset of the low-energy samples, and (ii) the updating strategy as a function of the expectation value, i.e., $h_j^b(\langle\sigma_j^z\rangle)$ (depicted in (**c**)).

solution fed into the quantum algorithm, leveraging the complexity and cost of the quantum routine while ensuring a better performance[71,72].

In BF-DCQO, the standard DCQO is performed iteratively, so that the solution from each step serves as the input bias for the next iteration[50,51,69]. See Fig. 1 for a schematic diagram of the protocol. The initial Hamiltonian is changed after each bias-field update,

$$\tilde{H}_i = H_i + \sum_{j=0}^{N-1} h_j^b(\langle\sigma_j^z\rangle)\sigma_j^z, \tag{8}$$

so that its ground state also changes and has to be prepared for the circuit execution. The smallest eigenvalue of the single-body operator $\left[h_i^x\sigma_i^x - h_i^b\sigma_i^z\right]$ is given by $\lambda_i^{\min} = -\sqrt{(h_i^b)^2 + (h_i^x)^2}$, and its associated eigenvector is $|\tilde{\phi}\rangle_i = R_y(\theta_i)|0\rangle_i$ where $\theta_i = 2\tan^{-1}\left(\frac{h_i^b + \lambda_{min}}{h_i^x}\right)$. Therefore, the ground state of $\tilde{H}_i$ can be prepared using N y-axis rotations as

$$|\tilde{\psi}_i\rangle = \bigotimes_{i=1}^{N}|\tilde{\phi}\rangle_i = \bigotimes_{i=1}^{N} R_y(\theta_i)|0\rangle_i. \tag{9}$$

In each iteration, the bias field h_j^b for the jth qubit is updated based on the measured longitudinal component of the qubit $\langle\sigma_j^z\rangle$. This update follows the rule $h_j^b = h_j^b(\langle\sigma_j^z\rangle)$, where the functional form of h_j^b represents the specific bias-field strategy employed. In this work, we explore the following strategies:

- Unsigned antibias(+)/bias(−): $h_j^b = \pm\langle\sigma_j^z\rangle$. This strategy offers bias fields whose strength is exactly the longitudinal component. This is a sensible choice when a qubit is effectively close to an equal superposition, such that there is no clear direction of bias.
- Signed antibias(+)/bias(−): $h_j^b = \pm\,\mathrm{sgn}\langle\sigma_j^z\rangle$. This strategy offers bias fields that are equivalent to the effective orientation of the qubit, regardless the magnitude. This is a sensible choice when a qubit has a clear preferred direction of bias.

Once a suitable updating method has been selected, BF-DCQO iteratively measures the final state after time evolution in the computational basis and the longitudinal bias fields h_j^b are updated accordingly. In the following, we set $h_j^b = 0$ for the first bias-field iteration. According to the findings of Ref. 51, modifying the selected updating strategy throughout the entire routine can circumvent local minima and lead to faster convergence. For our results, we use the unsigned bias followed by a final iteration with a weighted signed bias. Specifically, the strength of h_j^b is increased by rescaling $h_j^b \mapsto \kappa h_j^b$ with $\kappa > 0$. In our experiments, we rescale by a factor of five to ensure that the magnitude of the bias is significantly larger than the transverse term, restricting the search space near the previous solution. Since the solution provided by DCQO, from the first iteration, samples low-energy states of the spin-glass Hamiltonian [Eq. (1)], the expectation values of local Pauli-z operators can be used as an effective bias in subsequent iterations, facilitating convergence.

Although this updating strategy is employed in our experiments, alternative approaches might be more convenient depending on the nature of the problem at hand. Using $\kappa \in (0, 1)$ grants more importance to the transverse contribution in $\tilde{H}_i$, whose ground state is an equal superposition of the computational basis. Thereby, a broader energy landscape is explored by flattening the expected sampling distribution. The algorithm is less prone to getting stuck in local minima with this choice, though it may significantly slow down convergence. On the other hand, using $\kappa > 1$ provides greater strength to the longitudinal bias-field update, i.e., the optimal solution obtained from the last BF-DCQO iteration, constraining the search space around this solution. This accelerates the convergence but may lead to an undesired local minimum.

Once the circuit has been executed, all qubits are measured n_{shots} times, returning an N-bitstring $x_0 \ldots x_{N-1}$. Each measurement trivially translates into a sample of H_f due to its construction as a weighted sum of Pauli-z operators. Denoting each of these samples as E_k, the sample mean energy is defined as $E = (1/n_{\text{shots}})\sum_{k=1}^{n_{\text{shots}}} E_k$. It can be used as an estimator of the expectation value of H_f after ground-state preparation.

It has been demonstrated that incorporating Conditional Value-at-Risk (CVaR) techniques into quantum optimization routines[73] can lead to significant improvements. Recent studies have explored the impact of noise when sampling bitstrings from quantum computers. They determined upper and lower bounds for noiseless expectation values using CVaR noisy samples and quantified the sampling overhead needed to achieve good solutions[43]. Building upon this knowledge, we propose a CVaR-inspired method for iteratively updating the bias fields. Accordingly, let α be the ratio between the number of measurements considered and the total number of shots n_{shots}. Rather than taking the entire distribution of samples into account ($\alpha = 1$), we first sort them in terms of energy so that $E_k \leq E_{k+1}$. Next, the bias is updated using a fraction $0 < \alpha < 1$ of the lowest-energy outcomes taken from

$$E(\alpha) = \frac{1}{\lceil \alpha n_{\text{shots}} \rceil} \sum_{k=1}^{\lceil \alpha n_{\text{shots}} \rceil} E_k, \tag{10}$$

thus taking only a part of the total distribution into account. From the results drawn from both noiseless simulators and hardware, we find the fastest convergence to the best solutions for values of $\alpha \sim 1\%$. This value is found empirically and the optimal value will depend on the problem and the

number of shots. For example, we find that using smaller (larger) values of α shows faster convergence if the number of shots is large (small) with respect to the numbers used here.

Apart from seeking a reduction in the resources required and depth of the circuits considered, it is important to quantify the quality of the results obtained by the routines. In order to evaluate the performance of our routines, we use two metrics: the approximation ratio

$$\mathrm{AR} = \frac{E(\alpha = 1)}{E_0}, \tag{11}$$

and the distance to solution

$$\mathrm{DS} = 1 - \frac{\min\{E_k\}_{k=1}^{n_{\mathrm{shots}}}}{E_0}. \tag{12}$$

In all our studies of 156 and 433 qubits, the exact ground-state energies E_0 are obtained numerically by an iterative method similar to Ref. 74 (see Supplementary Note 2 for details). For 25-qubit instances, we obtain the exact solution using a brute force method.

HUBO instances considered

In this section, we present the HUBO Hamiltonians that are employed for testing BF-DCQO. Based on the gate error rates and on the coupling map connectivities of the selected platforms, we work with a nearest-neighbour three-body spin glass. In order to tackle industry-related use cases, we furthermore consider the weighted MAX 3-SAT problem[52]. To the best of our knowledge, this is the first work to tackle a binary satisfiability problem with the aid of CD protocols. For both cases, the corresponding circuit decomposition is shown in Supplementary Note 3.

Nearest-neighbour spin glass.—For the first case, the nearest-neighbour (NN) three-body Hamiltonian takes the form of

$$H_f^{\mathrm{NN}} = \sum_i h_i^z \sigma_i^z + \sum_{\langle ij\rangle} J_{ij}\sigma_i^z\sigma_j^z + \sum_{\langle ijk\rangle} K_{ijk}\sigma_i^z\sigma_j^z\sigma_k^z, \tag{13}$$

where $\langle\cdot\rangle$ indicates that the enclosed qubit indices are nearest neighbours in the one-dimensional chain (thus $j = i + 1$ and $k = i + 2$). The coupling constants h_i, J_{ij} and K_{ijk} are taken as random Gaussian-distributed numbers with zero mean and unit variance. The first-order nested-commutator expansion for this Hamiltonian is given by Eq. (6) but it only contains the nearest-neighbour qubit indices as in Eq. (13). Due to its linearity, it perfectly fits the heavy-hex IBM qubit coupling maps[75]. Furthermore, the ease with which this and related models can be simulated using tensor networks makes their simulation an ideal benchmark for evaluating the performance of quantum platforms. In addition to the 156-qubit experiment, we conduct a similar test consider a 433-qubit NN HUBO instance with the objective of simulating ideally (without noise) the expected performance of the upcoming IBM Osprey quantum platform via MPS.

Weighted MAX 3-SAT problem.—The maximum k-satisfiability (MAX k-SAT) problem belongs to the NP-complete complexity class[76] and its weighted variant is defined as follows: given a Boolean formula in conjunctive normal form (thus conjunction of disjuncted clauses), the weighted maximum k-satisfiability problem (MAX W-k-SAT) aims to find an assignment of truth-valued variables that maximizes the sum of weights of all the k-variable clauses met[52]. The MAX k-SAT problem can be recovered simply by setting the weights equal to one. If we let $k = 3$, this problem can be written as

$$C^{\mathrm{MW3S}}(l) = \bigwedge_{ijk} \omega_{ijk} l_i \vee l_j \vee l_k, \tag{14}$$

with l_i a literal representing a propositional variable, either u_i or its negation $\bar{u}_i$, and ω_{ijk} are the weights. The problem can be mapped into binary variables by performing the substitution $u_i \mapsto 1 - x_i$ and $\bar{u}_i \mapsto x_i$ with $x_i \in \{0, 1\}$. For each clause, the OR product of literals can be expanded into products of binary variables, e.g.,

$$u_i \vee \bar{u}_j \vee u_k \mapsto (1 - x_i)x_j(1 - x_k). \tag{15}$$

In order to address this problem with the aid of quantum computers, we perform an additional map turning the binary variables into Ising variables using the transformation $x_i \mapsto (I - \sigma_i^z)/2$.

Setting $c_i = 1$ if l_i is negated and $c_i = 0$ otherwise, we finally define the problem Hamiltonian as

$$H_f^{\mathrm{MW3S}} = \sum_{ijk} \frac{\omega_{ijk}}{8}[I + (-1)^{c_i}\sigma_i^z][I + (-1)^{c_j}\sigma_j^z][I + (-1)^{c_k}\sigma_k^z]. \tag{16}$$

Here, ω_{ijk} is chosen as a random uniformly distributed variable between zero and one. As this is a maximization problem, it can be transformed into a minimization one by performing the map $H_f^{\mathrm{MW3S}} \mapsto -H_f^{\mathrm{MW3S}}$. The first-order nested-commutator of Eq. (16) yields

$$\begin{aligned}\mathcal{O}_1^{\mathrm{MW3S}} = -i\sum_{ijk}\frac{\omega_{ijk}}{4}\Big[&(-1)^{c_i}\sigma_i^y[I + (-1)^{c_j}\sigma_j^z][I + (-1)^{c_k}\sigma_k^z] \\ &+ (-1)^{c_j}[I + (-1)^{c_i}\sigma_i^z]\sigma_j^y[I + (-1)^{c_k}\sigma_k^z] \\ &+ (-1)^{c_k}[I + (-1)^{c_i}\sigma_i^z][I + (-1)^{c_j}\sigma_j^z]\sigma_k^y\Big].\end{aligned} \tag{17}$$

It can be seen that MAX W-3-SAT is in general a highly nonlocal Hamiltonian and thus is challenging to implement. We consider here the NN version of the MAX W-3-SAT Hamiltonian of Eq. (16), where consecutive indices are summed over as in Eq. (13). This model is similar to the nearest-neighbour spin-glass Hamiltonian H_f^{NN} but with additional next-to-nearest neighbour terms, namely $\sigma_i^z\sigma_{i+2}^z$, which makes it more complex to implement. In essence, this is due to the fact that such terms are seen as three-body interactions for a heavy-hex lattice, where an additional number of entangling gates are needed to couple distant qubits.

In contrast to physical phase transitions, where variations of the system parameters lead to qualitative changes in its properties, in computer science, computational phase transitions occur at critical points where algorithms require an increasing amount of computational resources, becoming less and less tractable[77]. The computational phase transitions of k-SAT have been the subject of several works[77–79]. They depend critically on the density of the problem, i.e., the ratio between its clauses and variables. For random 3-SAT instances, it has been proven that the critical point is located around a density of $\alpha_C = 4.3$.

von Neumann entanglement entropy

The role of entanglement in quantum optimization is an interesting question that has been discussed recently in the context of adiabatic[80,81] and variational[82–86] algorithms, with no clear consensus. Here, we study how entanglement changes with each bias-field iteration, by means of MPS simulations, to support our understanding of how BF-DCQO converges to the final solution.

The entanglement between two subsystems, in the case of a composite pure state, can be quantified by the von Neumann entropy of the reduced density matrix of either subsystem. In an MPS representation of the wavefunction[87], the entanglement entropy for any bipartition is given by the singular values corresponding to the bond that connects the two parts. For bond index i, we denote the jth-largest singular value by λ_{ij}. Here, j has values $j \in \{1, 2, \ldots, \chi_i\}$ up to the bond dimension χ_i and the bonds between qubits (tensors in the MPS) are indexed by $i \in \{1, \ldots, N-1\}$. We consider the entanglement entropy averaged over bonds

$$S = -\frac{1}{N-1}\sum_{i=1}^{N-1}\sum_{j=1}^{\chi_i}\lambda_{ij}^2\log_2\lambda_{ij}^2. \tag{18}$$

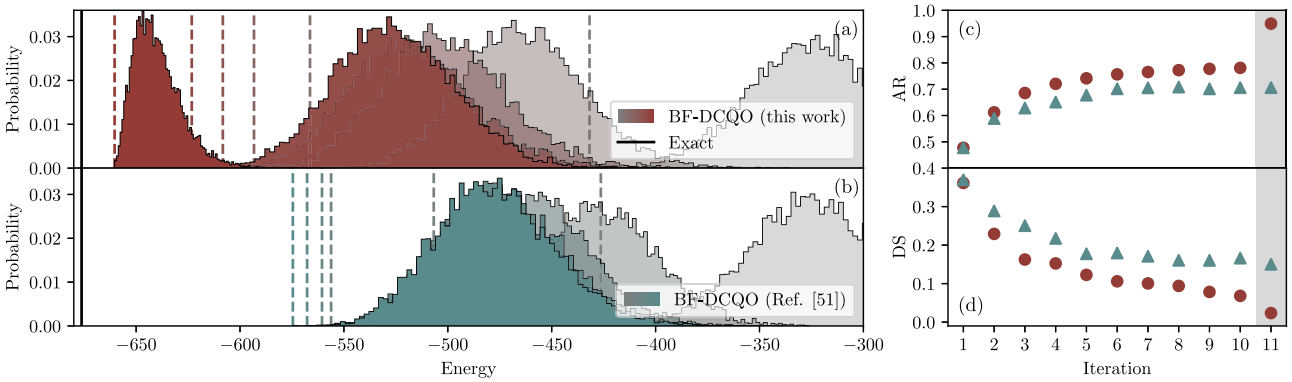

Fig. 2 | Performance comparison of the BF-DCQO variants for the 433-qubit NN HUBO results simulated via MPS. a Energy distributions for iterations 1, 3, 5, 7, 9 and 11; from grey to maroon using our novel BF-DCQO variant. The continuous line corresponds to the exact ground-state energy E_0 given by an iterative method [Supplementary Note 2], and the dashed lines correspond to the minima obtained from the distributions. Here, we report energies in units of the standard deviation of the coupling constants in Eq. (13). **b** Same plot as (**a**), going from grey to teal, but considering the original BF-DCQO approach[51]. **c**, **d** Approximation ratios and distances to solution obtained for each iteration for both approaches. For both panels and only for our variant (maroon markers), the shaded area indicates that the bias update is changed from unsigned to signed bias in the last iteration. See Table 1.

Table 1 | 433-qubit NN HUBO resources needed and results simulated via MPS

Iteration	X		$\sqrt{X}$		RZ(θ)		CZ		Depth		AR		DS	
1	497	497	5910	5910	5934	5934	2275	2275	99	99	0.477	0.477	0.361	0.370
2	470	453	5563	5421	5525	5379	2156	2108	98	98	0.612	0.589	0.229	0.289
3	466	446	5412	5310	5365	5247	2106	2066	98	98	0.686	0.628	0.163	0.251
4	436	427	5314	5314	5254	5261	2063	2065	98	98	0.720	0.651	0.152	0.218
5	455	441	5283	5310	5240	5242	2052	2063	98	98	0.741	0.678	0.123	0.178
6	479	450	5287	5310	5238	5251	2052	2063	98	98	0.756	0.702	0.106	0.180
7	474	448	5287	5301	5247	5207	2052	2061	99	98	0.765	0.705	0.101	0.171
8	455	435	5283	5301	5198	5226	2052	2061	98	99	0.772	0.708	0.094	0.161
9	464	456	5283	5310	5210	5251	2052	2063	98	98	0.777	0.701	0.078	0.161
10	447	447	5284	5277	5210	5214	2052	2052	99	98	0.781	0.706	0.068	0.166
11	100	456	1879	5283	1653	5225	496	2052	80	97	0.949	0.706	0.023	0.150

We compare both our BF-DCQO variant (left columns) and the original approach (right columns) with $n_{\text{shots}} = 10000$ and $\theta_{\text{cutoff}} = 0.06$. For our variant, we used $\alpha = 0.01$ and we performed a signed bias in the last iteration.

This quantity is minimally zero when the state is a product state and has an upper bound $\sim \log_2 2^N = N$ when the reduced density matrix of either subsystem is maximally mixed[88]. While entanglement generally scales with the subsystem volume, in special cases, stricter bounds such as area laws can be derived[89,90]. Nonequilibrium states resulting from global parameter quenches are expected to follow a volume law, though recent quantum simulations of paramagnetic-to-spin-glass quench dynamics exhibited area-law scaling[34]. Here, we do not analyze the scaling behavior but rather focus on the entanglement generated in the short-time dynamics of the counterdiabatically driven systems, as discussed in Entanglement in the iterative optimization.

Results and discussion

Enhanced BF-DCQO

In the following lines, we perform a comparison of the original BF-DCQO approach[51] and our proposed variant. We study a 433-qubit NN HUBO instance [Eq. (13)], using MPS to simulate the expected performance of the upcoming IBM Osprey quantum platform without noise. In this case, the values $n_{\text{shots}} = 10000$ and $\theta_{\text{cutoff}} = 0.06$ are set for both approaches and $\alpha = 0.01$ for our variant. The results can be seen in Fig. 2 and the amount of resources needed per iteration in Table 1. Figure 2 shows that before applying the signed bias, we obtain a 10.6% enhancement of the AR and 59.1% for the DS, demonstrating that our new CVaR-based approach for updating the bias fields provides a better performance than standard BF-DCQO. After the signed-bias method is applied in the last iteration for our variant, these values increase to 34.4% and 84.4%, respectively, showing that this additional feature remarkably contributes to improving the results obtained from standard BF-DCQO.

In addition, we find as an intrinsic signature of our BF-DCQO variant that the circuits implemented for each iteration require less and less resources even while the outcomes are more optimal. Conceptually, the goal of BF-DCQO is to encode the ground state of H_f, which can be either a product state in the computational basis or a superposition of them if the optimal solution is degenerate. For the first case—a separable state with no entanglement—BF-DCQO pushes the energy distribution towards the preparation of this state, reducing the amount of entanglement required per iteration. This feature indicates that BF-DCQO returns a lower-resource-demanding circuit per iteration, yielding a more classically tractable instance. Therefore, the combination of both quantum and classical computation paradigms appears like a promising route to address optimization problems by means of our BF-DCQO protocol. In the case of a superposition ground state, entanglement might still be reduced depending on the instance. We discuss the reduction of entanglement in more detail in Entanglement in the iterative optimization.

Comparison of methods

In order to assess the potential of our proposed BF-DCQO variant, we conduct a comprehensive benchmark study comparing it against several

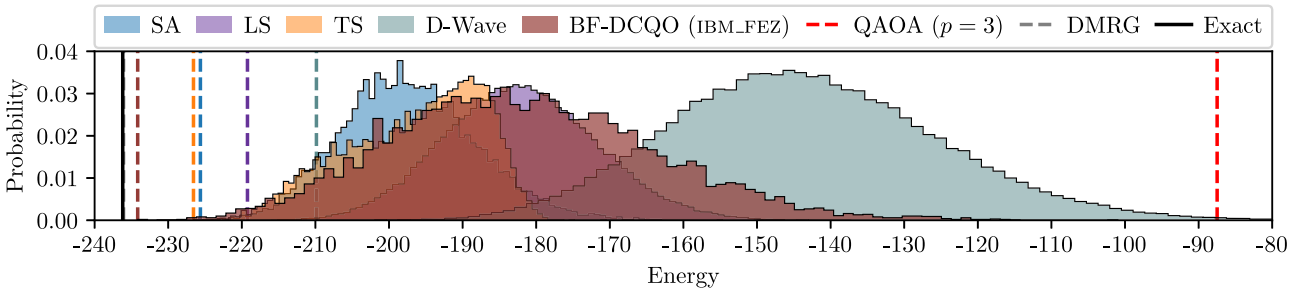

Fig. 3 | 156-qubit NN HUBO instance under different approaches. We solve Eq. (13) considering simulated annealing (SA, blue), local search algorithm (LS, purple), Tabu search (TS, orange), D-Wave (green), BF-DCQO om IBM_FEZ (maroon), the best outcome of QAOA up to $p = 3$ layers (dashed red), DMRG solution (dashed grey) and the exact solution (black line). The last two mostly overlap as DMRG reaches a nearly optimal solution [Supplementary Note 4]. The dashed vertical lines indicate the minimum energy values obtained for each approach. The D-Wave and BF-DCQO distributions correspond to experiments run on quantum hardware. Energies are in units the standard deviation of the coupling constants in Eq. (13).

well-established classical optimization techniques as well as the D-Wave platform. In particular, we optimize the nearest-neighbour three-body spin glass of Eq. (13) using a 156-qubit instance.

The results are presented in Fig. 3, where the methods and parameters are given by:

- Simulated annealing (SA)[91] with 100000 number of reads, initial (final) temperature $T_i = 2$ ($T_f = 0.05$) using a geometric cooling scheduling with 1000 sweeps.
- Local search (LS) algorithm, which can be seen as SA with zero-temperature Metropolis-Hastings criterion[92,93], with 100000 reads and 10000 sweeps.
- Tabu search (TS)[94] with 100000 reads starting from randomly generated initial states.
- D-Wave quantum annealers using ADVANTAGE_SYSTEM4.1 with an annealing time of 2000 μs and $n_{\text{shots}} = 100000$. Based on Ref. 42, we set a coupling strength that is two times the largest coupling of Eq. (1) in absolute value. We thereby introduce a penalty term after the HUBO-into-QUBO mapping when a product constraint is not met in the corresponding reduced spin glass model.
- Tenth iteration of BF-DCQO[51], with $\alpha = 0.02$ run on IBM_FEZ using $\theta_{\text{cutoff}} = 0.06$, $n_{\text{trot}} = 3$ and $n_{\text{shots}} = 10000$, ten times less than SA, TS and D-Wave to compensate the number of iterations. Previously, the ten BF-DCQO iterations were simulated using MPS without noise.
- CVaR-QAOA[4,73] with $p = 3$ layers, $n_{\text{shots}} = 10000$ and $\alpha = 0.1$ via MPS using the SPSA optimizer.
- The DMRG implementation of the ITensor library[95]. We find convergence with 10 sweeps, maximum bond dimension 10, truncation error cutoff of 10^{-10}, and a noise parameter that is gradually reduced from 10^{-3} to zero through the sweeps (see Supplementary Note 4).
- Exact solution using a numerical iterative method [Supplementary Note 2].

Figure 3 illustrates that BF-DCQO is capable of outperforming other established methods on current noisy quantum platforms, returning an energy distribution whose minimum outcome is very close to the exact ground state energy. In particular, we have obtained a 26.7% enhancement of the AR and 92.3% of the DS metrics with respect to D-Wave and a 71.7% enhancement of DS for SA approach but a small -8.0% lowering for the AR metric. Despite the fact that three layers were chosen for CVaR-QAOA to recover the expected behaviour of BF-DCQO with $n_{\text{trot}} = 3$, the obtained results show the worst performance, even in comparison with D-Wave. This finding is in accordance with the results presented in Ref. 42. Furthermore, it should be noted that BF-DCQO and QAOA do not suffer from the inherent qubit overhead required for mapping HUBO into QUBO problems, as D-Wave does. In addition, as the order of many-body terms in the problem Hamiltonian H_f increases, the qubit overhead increases and more resources are required. In particular, regular quadratization methods require a number of ancillary qubits proportional to $n_{k\text{-body}}(k-2)$, with $n_{k\text{-body}}$ the number of k-body terms of H_f[96–98]. Therefore, a worse performance is expected. Other known methods such as Gurobi[99] and CPLEX[100] also suffer from this drawback. For the results presented in Fig. 3, 334 variables were needed for D-Wave. This feature is absent in BF-DCQO, making it a suitable technique for working with large-scale optimization problems with minimal resource requirements.

Up to this point, we have compared the performance of BF-DCQO to other methods by simulating the entire BF-DCQO routine with MPS and running the circuit obtained in the last iteration on hardware. In the following section, the impact of running the entire routine under noisy environments is examined. To this end, larger values of θ_{cutoff} will be set in order to guarantee implementability. We note that considering a larger number of measurements might allow us to partially recover the lost expressivity due to the increase of θ_{cutoff}.

Hardware implementation on IBM

We first make use of the 156-qubit superconducting quantum platform IBM_FEZ with the native gate set $\{X, \sqrt{X}, \text{RZ}(\theta), \text{CZ}\}$ (see Supplementary Note 3). The linearity of its heavy-hex qubit coupling map encourages us to work with Hamiltonians whose many-body terms are nearest neighbours, thereby avoiding an overhead of entangling gates for coupling distant qubits. With this in mind, we solve the same 156-qubit NN HUBO instance that was previously tested in Fig. 3, but we now run the entire routine on IBM_FEZ. The computation is thus conducted in a purely quantum manner. We use $n_{\text{shots}} = 10{,}000$, $\alpha = 0.01$, $\theta_{\text{cutoff}} = 0.13$, and a total of eleven iterations, considering an unsigned-bias update for the first ten and a signed bias for the last one. The results are presented in Fig. 4, which depicts the iterative procedure of BF-DCQO and how the obtained outcomes move towards the desired solution. The amount of resources needed per iteration is given in Table 2.

As a final remark, the final iteration of the purely quantum BF-DCQO routine exhibits a slightly worse performance when compared to the results of Fig. 3, which employed a noiseless simulation with a considerably lower gate threshold. The purely quantum BF-DCQO still outperforms the optimal solution obtained on the D-Wave platform, where we obtained 34.1% of AR enhancement and 66.1% of DS enhancement with respect the experiment run on D-Wave in Fig. 3.

With the aim of solving more industrially relevant and denser large-scale problems, we also solve a 156-qubit NN MAX W-3-SAT instance on IBM_FEZ, described by Eq. (16) with only nearest-neighbour terms. We use the same parameters as for the previous instance but change $\theta_{\text{cutoff}} = 0.06$ for convenience. The results are shown in Fig. 5, and the amount of resources needed per iteration is listed in Table 3. For this particular problem, the best outcome obtained is quite close to the optimal solution despite a purely quantum routine, which highlights the efficacy of BF-DCQO under noisy environments. Additionally, we solved the same HUBO instance on D-Wave using $n_{\text{shots}} = 100000$. The purely quantum BF-DCQO again outperforms the D-Wave results: we obtain a 43.0% enhancement of the AR and an

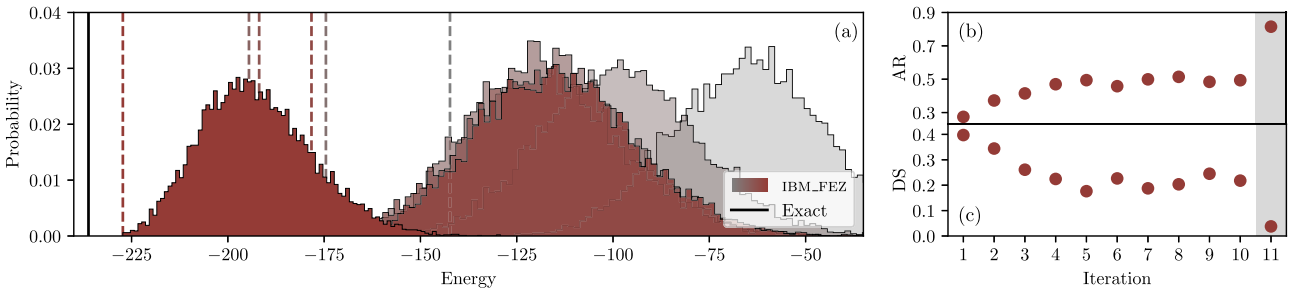

Fig. 4 | 156-qubit NN HUBO results on IBM_FEZ. a Energy distributions for iterations 1, 3, 5, 7, 9 and 11; from grey to maroon respectively. The continuous line corresponds to the exact ground state energy E_0 [Supplementary Note 2]. The dashed lines correspond to the minima obtained from the distributions. Energies are in units the standard deviation of the coupling constants in Eq. (13). **b**, **c** Approximation ratios and distances to solution for each iteration. For both panels, the shaded area indicates that the bias update is changed from unsigned to signed bias in the last iteration. See Table 2.

Table 2 | 156-qubit NN HUBO results and resources needed on IBM_FEZ

Iteration	X	$\sqrt{X}$	RZ(θ)	CZ	Depth	AR	DS
1	115	1020	1030	477	129	0.274	0.397
2	86	969	916	430	126	0.372	0.344
3	92	958	869	424	129	0.415	0.261
4	85	937	861	410	124	0.470	0.225
5	93	938	862	410	127	0.494	0.176
6	83	941	878	410	124	0.458	0.227
7	85	940	878	410	125	0.499	0.188
8	79	899	834	386	90	0.514	0.203
9	79	903	835	386	93	0.484	0.245
10	79	941	859	410	130	0.494	0.218
11	3	330	180	13	39	0.815	0.038

We consider n_{shots} = 10000, α = 0.01 and θ_{cutoff} = 0.13. At the last iteration, we performed signed bias.

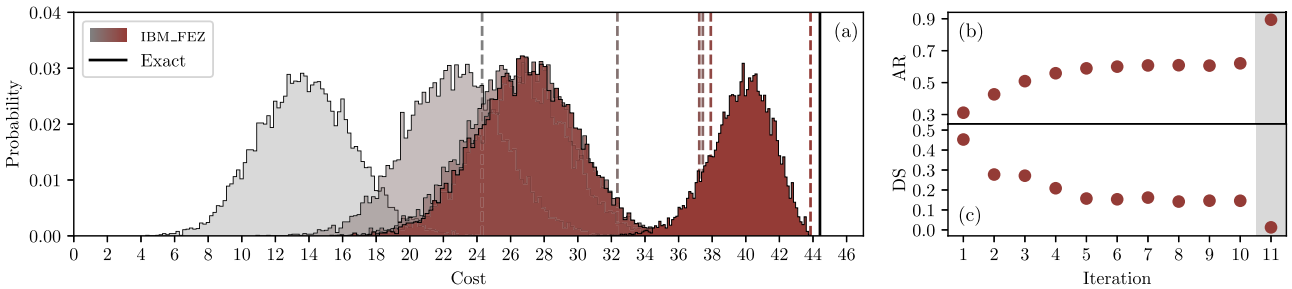

Fig. 5 | 156-qubit MAX W-3-SAT HUBO results on IBM_FEZ. a Cost function distributions for iterations 1, 3, 5, 7, 9 and 11; from grey to maroon respectively. The continuous line corresponds to the exact ground-state energy E_0 [Supplementary Note 2]. The cost function is in units of max(ω_{ijk}) in Eq. (16). The dashed lines correspond to the maxima of the distributions. **b**, **c** Approximation ratios and distances to solution obtained for each iteration. The shaded area indicates that the bias update is changed from unsigned to signed in the last iteration. See Table 3.

88.5% enhancement of the DS with respect the experiment run on the D-Wave platform.

Dense problems with all-to-all connectivity

The sparsity and high locality of the terms involved in the instances considered on IBM render the problems amenable to classical simulation. To evaluate the efficacy of BF-DCQO in more intricate scenarios with long-range couplings, we extend our analysis to denser versions of MAX 3-SAT. In particular, we set as clause-to-variable ratio the critical density for 3-SAT, $\alpha_C = 4.3$. Dense MAX 3-SAT instances with uniform couplings equal to unity are then generated randomly with the number of clauses given by $\lceil N\alpha_C \rceil$. It is important to note that the expected optimal solutions of MAX k-SAT instances, where clauses are uniformly weighted, can be either a product state or a low-entangled superposition of few bitstrings. As a last remark, optimal solution degeneracy was not present in our previous studies and it may compromise the performance.

We employ the 25-qubit IONQ ARIA 1 emulator with native gate set given by {MS(ϕ_0, ϕ_1, θ), GPi(ϕ), GPi2(ϕ)} (see Supplementary Note 3). It mimics an all-to-all connected trapped-ion platform and encompasses both noiseless and noisy simulations, applying debiased error mitigation[101] with a noise profile that matches the ARIA 1 expected performance. The system size of the problem allows to obtain the exact optimal solution to be obtained by our protocol. The results for

$n_{\text{shots}} = 1000$, $\alpha = 0.01$ and $\theta_{\text{cutoff}} = 0.06$ can be seen in Fig. 6, where the amount of resources required at each iteration presented in Table 4. The data shows that the BF-DCQO protocol is able to reach the exact optimal state in both noiseless and noisy environments at the second iteration, which serves to further validate the efficacy of the method.

Entanglement in the iterative optimization

The role of entanglement dynamics in quantum algorithms is an interesting and nontrivial question. In adiabatic quantum optimization, both the initial state and the desired final state are product states or low-entangled multipartite states, while the adiabatic path may explore highly entangled states[80,81]. To gain insight into our observation that the required number of entangling gates is reduced with increasing iterations, we consider the flow of entanglement along the dynamical process.

We compute the entanglement entropy of Eq. (18) for the 433-qubit NN and the 25-qubit dense MAX 3-SAT HUBO instances solved previously in Figs. 2 and 6. As mentioned before, the first case corresponds to a sparse problem with a nondegenerate optimal solution and the second one to a dense problem with a degenerate optimal solution. For the second case, we only consider the noisy simulation including debiased error mitigation [Fig. 6b]. We show, in Fig. 7, how the entanglement entropy decays with the subsequent BF-DCQO iterations for both problems. Due to the dense nonlocal couplings, the average entanglement entropy generated in the second instance is larger than in the first. The numbers of entangling gates used here are listed in Tables 1 and 4. We can see that for the second instance, in the first three iterations, the average entanglement entropy decreases even when the number of entangling gates remains the same. Similar to the AR and DS in Figs. 2 and 6, the entropy then nearly saturates up to the last iteration. The signed bias applied in the last iteration significantly reduces the number of entangling gates and the entanglement entropy drops to a value close to zero. This indicates that the iteration protocol produces a classical ground state as expected.

We note that while the entanglement entropy analyzed here is naturally obtained from the MPS representation, it is not a straightforward quantity to measure experimentally. In order to characterize entanglement in experiments run on quantum hardware, for instance in the case of highly entangled states not amenable to tensor network simulations, alternative measures would be required, such as correlator functions by means of quantum measurements[90,102].

Table 3 | 156-qubit NN MAX W-3-SAT HUBO results and resources needed on IBM_FEZ

Iteration	X	$\sqrt{X}$	RZ(θ)	CZ	Depth	AR	DS
1	88	1359	1309	495	189	0.311	0.453
2	39	949	808	285	103	0.426	0.277
3	2	450	296	64	23	0.509	0.271
4	3	427	271	56	23	0.559	0.209
5	0	421	267	50	23	0.589	0.157
6	2	411	265	50	19	0.600	0.153
7	2	416	267	50	23	0.608	0.162
8	2	417	263	50	23	0.609	0.142
9	2	412	252	50	18	0.606	0.146
10	2	417	261	50	22	0.621	0.146
11	-	311	156	-	4	0.894	0.013

We consider $n_{\text{shots}} = 10000$, $\alpha = 0.01$, and $\theta_{\text{cutoff}} = 0.06$. In the last iteration, we apply a signed bias, where no entangling gates are used.

Conclusions

In this study, we investigate and evaluate the performance of variants of the recently proposed BF-DCQO algorithm[51] by solving large-scale HUBO instances on IBM quantum processors and IonQ noisy emulators. The superiority of our BF-DCQO variant over well-established classical techniques and optimization on the D-Wave ADVANTAGE_SYSTEM4.1 is verified through computing the approximation ratio and the distance to solution in an iterative process. We obtain better optimal solutions even while the circuits after each iteration demand less resources. This is achieved by means of an iterative learning procedure, where the optimal solutions obtained from the last iteration are used for the subsequent one, providing several techniques to guarantee convergence under different scenarios. Furthermore, in order to address not only the current but also the near-term hardware, we examine the expected performance of BF-DCQO on the upcoming IBM Osprey platform with 433 qubits. Simulating 433-qubit HUBO instances without noise yields promising results. The BF-DCQO algorithm does not require any classical optimization subroutines, thus avoiding potential trainability drawbacks, nor does it require extra qubits for mapping the initial HUBO into a QUBO problem.

We provide numerical evidence of how our protocol disentangles the states obtained after each iteration, one of the key signatures of our method. This feature enables an iterative reduction in the number of resources required, thus making subsequent circuits more classically tractable and opening the door to employing hybrid quantum-classical strategies. Therefore, the BF-DCQO algorithm emerges as a suitable algorithm for solving higher-order binary optimization problems on both current and

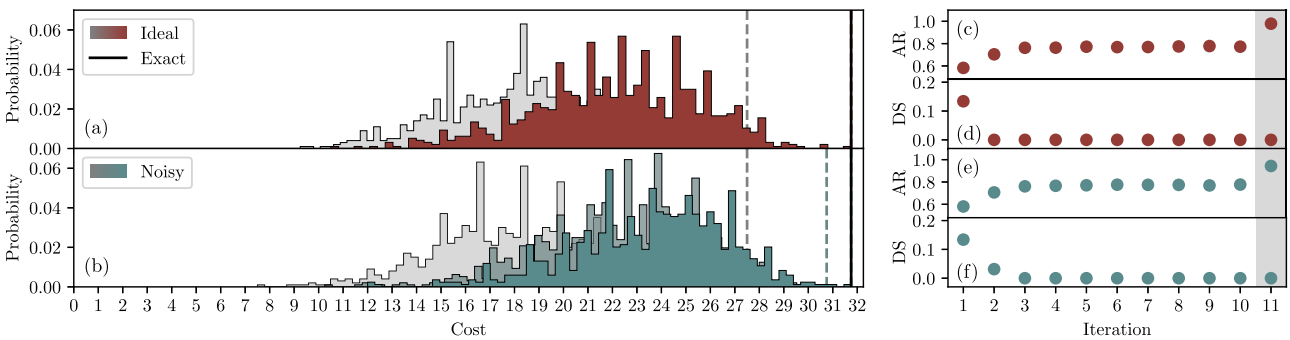

Fig. 6 | 25-qubit dense MAX 3-SAT HUBO results on IONQ ARIA 1 emulator. **a**, **b** Cost function distributions for the first two and three iterations without noise (grey to maroon) and including an IONQ ARIA 1 noise model profile plus debiased error mitigation (grey to teal), respectively. The exact ground state (continuous line) is reached for both scenarios. The dashed lines correspond to the maximum cost obtained from the distributions. The cost function is in units of the coupling ω_{ijk} in Eq. (16), which here is chosen as uniform. **c**–**f** approximation ratios and distance to solution for both ideal and noisy emulations, respectively. Shaded areas indicate that the bias updating is changed from unsigned to signed bias at the last iteration. See Table 4.

Table 4 | 25-qubit dense MAX 3-SAT HUBO results and resources needed on IONQ ARIA 1 emulator

Iteration	MS(ϕ_0, ϕ_1, θ)		GPi(ϕ)		GPi2(ϕ)		Depth		AR		DS	
1	96	96	282	282	948	948	219	219	0.582	0.580	0.134	0.134
2	96	96	282	282	948	948	219	219	0.704	0.707	0.000	0.031
3	96	96	282	282	948	948	219	219	0.763	0.761	0.000	0.000
4	96	96	282	282	948	948	219	219	0.764	0.766	0.000	0.000
5	96	96	282	282	948	948	219	219	0.772	0.770	0.000	0.000
6	96	96	282	282	948	948	219	219	0.769	0.776	0.000	0.000
7	96	96	282	282	948	948	219	219	0.769	0.775	0.000	0.000
8	96	96	282	282	948	948	219	219	0.775	0.774	0.000	0.000
9	96	96	282	282	948	948	219	219	0.778	0.769	0.000	0.000
10	96	96	282	282	948	948	219	219	0.773	0.777	0.000	0.000
11	-	-	26	26	52	52	7	7	0.979	0.943	0.000	0.000

Noiseless (left) and IONQ ARIA 1-noise profile with debiased error mitigation (right) simulations are considered with $n_{shots} = 1000$, $\alpha = 0.01$ and $\theta_{cutoff} = 0.06$. At the last iteration, we performed signed bias, where no entangling gates were used.

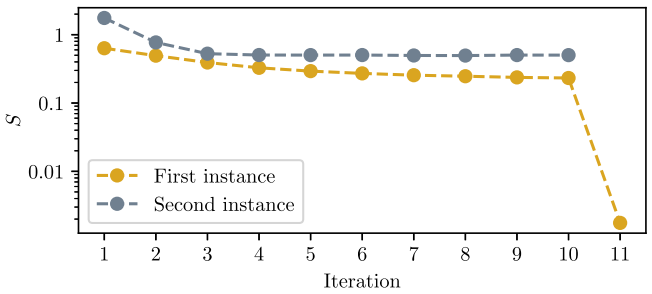

Fig. 7 | Average entanglement entropy S as a function of the iteration. The first instance corresponds to 433-qubit NN HUBO problem and the second instance to a 25-qubit dense MAX 3-SAT HUBO problem. Signed bias is applied at the last iteration, significantly reducing the number of entangling gates used and consequently the entanglement entropy. For the second instance, the entanglement entropy drops to zero at the last iteration as there are no entangling gates. We therefore leave out the last data point.

near-term quantum platforms, paving the path towards solving large-scale optimization problems with status-quo and next-generation quantum processors.

Data availability

Data is available from the corresponding author upon reasonable request.

Code availability

The codes used to generate data for this paper are available from the corresponding author upon reasonable request.

Received: 16 March 2025; Accepted: 11 August 2025;
Published online: 23 August 2025

References

1. Fu, Y. & Anderson, P. W. Application of statistical mechanics to NP-complete problems in combinatorial optimisation. *J. Phys. A Math. Gen.* **19**, 1605 (1986).
2. Lucas, A. Ising formulations of many NP problems. *Front. Phys.* **2**, 5 (2014).
3. Albash, T. & Lidar, D. A. Adiabatic quantum computation. *Rev. Mod. Phys.* **90**, 015002 (2018).
4. Farhi, E., Goldstone, J. & Gutmann, S. *A Quantum Approximate Optimization Algorithm* (2014), arXiv:1411.4028 [quant-ph].
5. Barends, R. et al. Digitized adiabatic quantum computing with a superconducting circuit. *Nature* **534**, 222–226 (2016).
6. Durr, C. & Hoyer, P. *A Quantum Algorithm for Finding the Minimum* (1999), arXiv:quant-ph/9607014 [quant-ph].
7. Montanaro, A. Quantum-walk speedup of backtracking algorithms. *Theory Comput.* **14**, 1 (2018).
8. Montanaro, A. Quantum speedup of branch-and-bound algorithms. *Phys. Rev. Res.* **2**, 013056 (2020).
9. Chakrabarti, S., Minssen, P., Yalovetzky, R. & Pistoia, M. *Universal Quantum Speedup for Branch-and-Bound, Branch-and-Cut, and Tree-Search Algorithms* (2022), arXiv:2210.03210 [quant-ph].
10. Somma, R. D., Boixo, S., Barnum, H. & Knill, E. Quantum simulations of classical annealing processes. *Phys. Rev. Lett.* **101**, 130504 (2008).
11. Wocjan, P. & Abeyesinghe, A. Speedup via quantum sampling. *Phys. Rev. A* **78**, 042336 (2008).
12. Hastings, M. B. A short path quantum algorithm for exact optimization. *Quantum* **2**, 78 (2018).
13. Dalzell, A. M., Pancotti, N., Campbell, E. T. & Brandão, F. G. Mind the Gap: Achieving a Super-Grover Quantum Speedup by Jumping to the End, *Proceedings of the 55th Annual ACM Symposium on Theory of Computing*, STOC, p. 1131-1144 (Association for Computing Machinery, New York, 2023).
14. Boulebnane, S. & Montanaro, A. Solving Boolean satisfiability problems with the quantum approximate optimization algorithm. *PRX Quantum* **5**, 030348 (2024).
15. Boehmer, A. Binary pulse compression codes. *IEEE Trans. Inf. Theory* **13**, 156 (1967).
16. Schroeder, M. Synthesis of low-peak-factor signals and binary sequences with low autocorrelation (Corresp.). *IEEE Trans. Inf. Theory* **16**, 85 (1970).
17. Shaydulin, R. et al. Evidence of scaling advantage for the quantum approximate optimization algorithm on a classically intractable problem. *Sci. Adv.* **10**, eadm6761 (2024).
18. Orús, R. A practical introduction to tensor networks: Matrix product states and projected entangled pair states. *Ann. Phys.* **349**, 117 (2014).
19. Silvi, P. et al. The Tensor Networks Anthology: Simulation techniques for many-body quantum lattice systems. *SciPost Phys. Lect. Notes*, **8** (2019).
20. Ran, S.-J. et al. *Tensor network contractions: methods and applications to quantum many-body systems*, Vol. 964 (Springer Nature, 2020).

21. Cirac, J. I., Pérez-García, D., Schuch, N. & Verstraete, F. Matrix product states and projected entangled pair states: Concepts, symmetries, theorems. *Rev. Mod. Phys.* **93**, 045003 (2021).
22. Bañuls, M. C. Tensor network algorithms: a route map. *Annu. Rev. Condens. Matter Phys.* **14**, 173 (2023).
23. Orús, R. Tensor networks for complex quantum systems. *Nat. Rev. Phys.* **1**, 538 (2019).
24. Lin, S.-H., Dilip, R., Green, A. G., Smith, A. & Pollmann, F. Real- and imaginary-time evolution with compressed quantum circuits. *PRX Quantum* **2**, 010342 (2021).
25. Rudolph, M. S. et al. Synergistic pretraining of parametrized quantum circuits via tensor networks. *Nat. Commun.* **14**, 8367 (2023).
26. Anselme Martin, B., Ayral, T., Jamet, F., Rančić, M. J. & Simon, P. Combining matrix product states and noisy quantum computers for quantum simulation. *Phys. Rev. A* **109**, 062437 (2024).
27. Berry, D. W. et al. Rapid Initial-State Preparation for the Quantum Simulation of Strongly Correlated Molecules. *PRX Quantum* **6**, 020327 (2025).
28. Kim, Y. et al. Evidence for the utility of quantum computing before fault tolerance. *Nature* **618**, 500–505 (2023).
29. Tindall, J., Fishman, M., Stoudenmire, E. M. & Sels, D. Efficient tensor network simulation of IBM's Eagle kicked Ising experiment. *PRX Quantum* **5**, 010308 (2024).
30. Begušić, T., Gray, J. & Chan, G. K.-L. Fast and converged classical simulations of evidence for the utility of quantum computing before fault tolerance. *Sci. Adv.* **10**, eadk4321 (2024).
31. Patra, S., Jahromi, S. S., Singh, S. & Orús, R. Efficient tensor network simulation of IBM's largest quantum processors. *Phys. Rev. Res.* **6**, 013326 (2024).
32. Liao, H.-J., Wang, K., Zhou, Z.-S., Zhang, P. & Xiang, T. *Simulation of IBM's kicked Ising experiment with Projected Entangled Pair Operator* (2023), arXiv:2308.03082 [quant-ph].
33. King, A. D. et al. Quantum critical dynamics in a 5,000-qubit programmable spin glass. *Nature* **617**, 61–66 (2023).
34. King, A. D. et al. Beyond-classical computation in quantum simulation. *Science* **388**, 199 (2025).
35. Han, Z.-Y., Wang, J., Fan, H., Wang, L. & Zhang, P. Unsupervised generative modeling using matrix product states. *Phys. Rev. X* **8**, 031012 (2018).
36. Lopez-Piqueres, J., Chen, J. & Perdomo-Ortiz, A. Symmetric tensor networks for generative modeling and constrained combinatorial optimization. *Mach. Learn. Sci. Technol.* **4**, 035009 (2023).
37. Alcazar, J., Ghazi Vakili, M., Kalayci, C. B. & Perdomo-Ortiz, A. Enhancing combinatorial optimization with classical and quantum generative models. *Nat. Commun.* **15**, 2761 (2024).
38. Mugel, S. et al. Dynamic portfolio optimization with real datasets using quantum processors and quantum-inspired tensor networks. *Phys. Rev. Res.* **4**, 013006 (2022).
39. Hao, T., Huang, X., Jia, C. & Peng, C. A Quantum-Inspired Tensor Network Algorithm for Constrained Combinatorial Optimization Problems, *Front. Phys.* **10**, https://doi.org/10.3389/fphy.2022.906590 (2022).
40. Patra, S., Singh, S. & Orús, R. Projected entangled pair states with flexible geometry. *Phys. Rev. Res.* **7**, L012002 (2025).
41. Pelofske, E., Bärtschi, A. & Eidenbenz, S. Quantum Annealing vs. QAOA: 127 Qubit Higher-Order Ising Problems on NISQ Computers, in *High Performance Computing: 38th International Conference, ISC High Performance 2023, Hamburg, Germany, May 21–25, 2023, Proceedings*, Lecture Notes in Computer Science, Vol. 13944, pp. 240–258 (Springer Nature Switzerland, Cham, 2023).
42. Pelofske, E., Bärtschi, A. & Eidenbenz, S. Short-depth QAOA circuits and quantum annealing on higher-order Ising models. *npj Quantum Inf.* **10**, 1–19 (2024).
43. Barron, S. V. et al. Provable bounds for noise-free expectation values computed from noisy samples. *Nat. Comput. Sci.* **4**, 865–875 (2024).
44. Sachdeva, N. et al. *Quantum optimization using a 127-qubit gate-model IBM quantum computer can outperform quantum annealers for nontrivial binary optimization problems* (2024), arXiv:2406.01743 [quant-ph].
45. Demirplak, M. & Rice, S. A. Adiabatic population transfer with control fields. *J. Phys. Chem. A* **107**, 9937 (2003).
46. Berry, M. V. Transitionless quantum driving. *J. Phys. A: Math. Theor.* **42**, 365303 (2009).
47. Chen, X., Ruschhaupt, A., Schmidt, S., del Campo, A., Guéry-Odelin, D. & Muga, J. G. Fast optimal frictionless atom cooling in harmonic traps: shortcut to adiabaticity. *Phys. Rev. Lett.* **104**, 063002 (2010).
48. del Campo, A. Shortcuts to adiabaticity by counterdiabatic driving. *Phys. Rev. Lett.* **111**, 100502 (2013).
49. Chandarana, P. et al. Digitized-counterdiabatic quantum approximate optimization algorithm. *Phys. Rev. Res.* **4**, 013141 (2022).
50. Hegade, N. N., Chen, X. & Solano, E. Digitized counterdiabatic quantum optimization. *Phys. Rev. Res.* **4**, L042030 (2022).
51. Cadavid, A. G., Dalal, A., Simen, A., Solano, E. & Hegade, N. N. Bias-field digitized counterdiabatic quantum optimization. *Phys. Rev. Res.* **7**, L022010 (2025).
52. Battiti, R. Maximum satisfiability problem, in *Encyclopedia of Optimization*, edited by Floudas, C. A. and Pardalos, P. M. pp. 2035–2041 (Springer US, Boston, MA, 2009).
53. Hegade, N. N., Paul, K., Albarrán-Arriagada, F., Chen, X. & Solano, E. Digitized adiabatic quantum factorization. *Phys. Rev. A* **104**, L050403 (2021).
54. Robert, A., Barkoutsos, P. K., Woerner, S. & Tavernelli, I. Resource-efficient quantum algorithm for protein folding. *npj Quantum Inf.* **7**, 1–5 (2021).
55. Chandarana, P., Hegade, N. N., Montalban, I., Solano, E. & Chen, X. Digitized counterdiabatic quantum algorithm for protein folding. *Phys. Rev. Appl.* **20**, 014024 (2023).
56. Gardner, E. Spin glasses with p-spin interactions. *Nucl. Phys. B* **257**, 747 (1985).
57. Kolodrubetz, M., Sels, D., Mehta, P. & Polkovnikov, A. Geometry and non-adiabatic response in quantum and classical systems. *Phys. Rep.* **697**, 1 (2017).
58. Sels, D. & Polkovnikov, A. Minimizing irreversible losses in quantum systems by local counterdiabatic driving. *Proc. Natl Acad. Sci. USA* **114**, E3909 (2017).
59. Claeys, P. W., Pandey, M., Sels, D. & Polkovnikov, A. Floquet-engineering counterdiabatic protocols in quantum many-body systems. *Phys. Rev. Lett.* **123**, 090602 (2019).
60. Hatomura, T. & Takahashi, K. Controlling and exploring quantum systems by algebraic expression of adiabatic gauge potential. *Phys. Rev. A* **103**, 012220 (2021).
61. Takahashi, K. & del Campo, A. Shortcuts to Adiabaticity in Krylov Space. *Phys. Rev. X* **14**, 011032 (2024).
62. Romero, S. V., Chen, X., Platero, G. & Ban, Y. Optimizing edge-state transfer in a Su-Schrieffer-Heeger chain via hybrid analog-digital strategies. *Phys. Rev. Appl.* **21**, 034033 (2024).
63. Dalal, A. et al. Digitized counterdiabatic quantum algorithms for logistics scheduling. *Phys. Rev. Appl.* **22**, 064068 (2024).
64. Hormozi, L., Brown, E. W., Carleo, G. & Troyer, M. Nonstoquastic Hamiltonians and quantum annealing of an Ising spin glass. *Phys. Rev. B* **95**, 184416 (2017).
65. Hegade, N. N. et al. Shortcuts to adiabaticity in digitized adiabatic quantum computing. *Phys. Rev. Appl.* **15**, 024038 (2021).
66. Suzuki, M. Fractal decomposition of exponential operators with applications to many-body theories and Monte Carlo simulations. *Phys. Lett. A* **146**, 319 (1990).

67. Sriluckshmy, P. V. et al. Optimal, hardware native decomposition of parameterized multi-qubit Pauli gates. *Quantum Sci. Technol.* **8**, 045029 (2023).
68. Algaba, M. G., Sriluckshmy, P. V., Leib, M. & Šimkovic IV, F. Low-depth simulations of fermionic systems on square-grid quantum hardware. *Quantum* **8**, 1327 (2024).
69. Graß, T. Quantum annealing with longitudinal bias fields. *Phys. Rev. Lett.* **123**, 120501 (2019).
70. Grass, T. Quantum annealing sampling with a bias field. *Phys. Rev. Appl.* **18**, 044036 (2022).
71. Egger, D. J., Mareček, J. & Woerner, S. Warm-starting quantum optimization. *Quantum* **5**, 479 (2021).
72. Truger, F. et al. Warm-starting and quantum computing: a systematic mapping study. *ACM Comput. Surv.* **56**, 1 (2024).
73. Barkoutsos, P. K., Nannicini, G., Robert, A., Tavernelli, I. & Woerner, S. Improving variational quantum optimization using CVaR. *Quantum* **4**, 256 (2020).
74. Gardner, E. & Derrida, B. Zero temperature magnetization of a one-dimensional spin glass. *J. Stat. Phys.* **39**, 367–377 (1985).
75. Chamberland, C., Zhu, G., Yoder, T. J., Hertzberg, J. B. & Cross, A. W. Topological and subsystem codes on low-degree graphs with flag qubits. *Phys. Rev. X* **10**, 011022 (2020).
76. Impagliazzo, R. & Paturi, R. On the complexity of k-SAT. *J. Comput. Syst. Sci.* **62**, 367–375 (2001).
77. Philathong, H., Akshay, V., Sambarskaya, K. & Biamonte, J. Computational phase transitions: benchmarking Ising machines and quantum optimisers. *J. Phys.: Complex.* **2**, 011002 (2021).
78. Zhang, B., Sone, A. & Zhuang, Q. Quantum computational phase transition in combinatorial problems. *npj Quantum Inf.* **8**, 87 (2022).
79. Philathong, H., Akshay, V., Zacharov, I. & Biamonte, J. Computational phase transition signature in Gibbs sampling. *J. Phys.: Complex.* **4**, 045010 (2023).
80. Hauke, P., Bonnes, L., Heyl, M. & Lechner, W. Probing entanglement in adiabatic quantum optimization with trapped ions. *Front. Phys.* **3**, https://doi.org/10.3389/fphy.2015.00021 (2015).
81. Bauer, B., Wang, L., Pižorn, I. & Troyer, M., *Entanglement as a resource in adiabatic quantum optimization* (2015), arXiv:1501.06914 [cond-mat.dis-nn].
82. Dupont, M., Didier, N., Hodson, M. J., Moore, J. E. & Reagor, M. J. Entanglement perspective on the quantum approximate optimization algorithm. *Phys. Rev. A* **106**, 022423 (2022).
83. Dupont, M., Didier, N., Hodson, M. J., Moore, J. E. & Reagor, M. J. Calibrating the classical hardness of the quantum approximate optimization algorithm. *PRX Quantum* **3**, 040339 (2022).
84. Sreedhar, R. et al. *The Quantum Approximate Optimization Algorithm performance with low entanglement and high circuit depth* (2022), arXiv:2207.03404 [quant-ph].
85. Nakhl, A. C., Quella, T. & Usman, M. Calibrating the role of entanglement in variational quantum circuits. *Phys. Rev. A* **109**, 032413 (2024).
86. Santra, G. C., Roy, S. S., Egger, D. J. & Hauke, P. Genuine multipartite entanglement in quantum optimization. *Phys. Rev. A* **111**, 022434 (2025).
87. Schollwöck, U. The density-matrix renormalization group in the age of matrix product states. *Ann. Phys.* **326**, 96 (2011).
88. Nielsen, M. A. & Chuang, I. L., *Quantum Computation and Quantum Information: 10th Anniversary Edition*, 1st ed. (Cambridge University Press, 2012).
89. Eisert, J., Cramer, M. & Plenio, M. B. Colloquium: Area laws for the entanglement entropy. *Rev. Mod. Phys.* **82**, 277 (2010).
90. Srivastava, A. K., Müller-Rigat, G., Lewenstein, M. & Rajchel-Mieldzioć, G. Introduction to quantum entanglement in many-body systems, in *New Trends and Platforms for Quantum Technologies*, edited by Aguado, R., Citro, R., Lewenstein, M. & Stern, M. pp. 225–285 (Springer Nature Switzerland, Cham, 2024).
91. Kirkpatrick, S., Gelatt, C. D. & Vecchi, M. P. Optimization by Simulated Annealing. *Science* **220**, 671 (1983).
92. Metropolis, N., Rosenbluth, A. W., Rosenbluth, M. N., Teller, A. H. & Teller, E. Equation of State Calculations by Fast Computing Machines. *J. Chem. Phys.* **21**, 1087 (1953).
93. Hastings, W. K. Monte Carlo sampling methods using Markov chains and their applications. *Biometrika* **57**, 97 (1970).
94. Glover, F., Taillard, E. & de Werra, D. A user's guide to Tabu search. *Ann. Oper. Res.* **41**, 3 (1993).
95. Fishman, M., White, S. R. & Stoudenmire, E. M. The ITensor Software Library for Tensor Network Calculations. *SciPost Phys. Codebases*, **4** (2022).
96. Ishikawa, H. Transformation of General Binary MRF Minimization to the First-Order Case. *IEEE Trans. Pattern Anal. Mach. Intell.* **33**, 1234 (2011).
97. Anthony, M., Boros, E., Crama, Y. & Gruber, A. Quadratic reformulations of nonlinear binary optimization problems. *Math. Program.* **162**, 115–144 (2017).
98. Dattani, N. Quadratization in discrete optimization and quantum mechanics (2019), arXiv:1901.04405 [quant-ph].
99. Gurobi Optimization, LLC *Gurobi Optimizer Reference Manual* (2024).
100. Cplex, I. I. V12.10.0: User's Manual for CPLEX. *Int. Bus. Mach. Corporation* **46**, 157 (2009).
101. Maksymov, A., Nguyen, J., Nam, Y. & Markov, I., Enhancing quantum computer performance via symmetrization (2023), arXiv:2301.07233 [quant-ph].
102. Rossini, D., Andolina, G. M., Rosa, D., Carrega, M. & Polini, M. Quantum advantage in the charging process of Sachdev-Ye-Kitaev batteries. *Phys. Rev. Lett.* **125**, 236402 (2020).

Acknowledgements

We would like to thank Shubham Kumar for preparing the schematic figure. We also thank Gaurav Dev and Bhargava A. Balaganchi for fruitful discussions. We acknowledge the use of IBM Quantum services for this work. The views expressed are those of the authors and do not reflect the official policy or position of IBM or the IBM Quantum team.

Author contributions

E.S. and N.N.H. conceived and supervised the work. S.V.R., A.-M.V., A.G.C., and N.N.H. developed the theoretical framework. S.V.R., A.-M.V., A.G.C., and A.S. developed the codes for obtaining the benchmark and hardware results. S.V.R. and N.N.H. analyzed the results. All authors participated in the discussion of results and writing the manuscript.

Competing interests

The authors declare no competing interests.

Additional information

Supplementary information The online version contains supplementary material available at https://doi.org/10.1038/s42005-025-02270-3.

Correspondence and requests for materials should be addressed to Narendra N. Hegade.

Peer review information *Communications Physics* thanks Julien Gacon and the other anonymous reviewer(s) for their contribution to the peer review of this work.